Selective Excitation of Localized Spin-Wave Modes by Optically Pumped Surface Acoustic Waves

C. L. Chang,[1] R. R. Tamming,[1] T. J. Broomhall,[2] J. Janusonis,[1] P. W. Fry,[3] R. I. Tobey,[1,4,*] and T. J. Hayward[2]

[1]*Zernike Institute for Advanced Materials, University of Groningen, Groningen, The Netherlands*

[2]*Department of Materials Science and Engineering, University of Sheffield, Sheffield, United Kingdom*

[3]*Nanoscience and Technology Centre, University of Sheffield, Sheffield, United Kingdom*

[4]*Center for Integrated Nanotechnologies, Los Alamos National Laboratory, Los Alamos, USA*

We explore the feasibility of exciting localized spin-wave modes in ferromagnetic nanostructures using surface acoustic waves. The time-resolved Faraday effect is used to probe the magnetization dynamics of an array of nickel nanowires. The optical-pump pulse excites both spin-wave modes of the nanowires and acoustic modes of the substrate and we observe that, when the frequencies of these modes coincide, the amplitude of magnetization dynamics is substantially enhanced due to magnetoelastic coupling between the two. Notably, by tuning the magnitude of an externally applied magnetic field, optically excited surface acoustic waves can selectively excite either the upper or lower branches of a splitting in the nanowire's spin-wave spectrum, which micromagnetic simulations indicate is caused by localization of spin waves in different parts of the nanowire. Thus, our results indicate the feasibility of using acoustic waves to selectively excite spatially confined spin waves, an approach that may find utility in future magnonic devices where coherent structural deformations could be used as coherent sources of propagating spin waves.

I. INTRODUCTION

With CMOS technology reaching the end of its scaling potential [1], there is great interest in developing technologies that will allow further growth in the power and efficiency of computational hardware. Among these technologies, magnonic devices [2,3], in which information is transported and processed via the propagation and interaction of spin waves, are attractive candidates, since they can hypothetically perform computations without transporting electrical charge, thus increasing energy efficiency.

Unfortunately, while propagating spin waves does not require current flow, their excitation, which is typically achieved using optical pulses [4–8], the Oested field of microwave strip lines [9–11], or spin-torque effects [12–14], is more problematic. Here, the former approach is limited by the difficulties of miniaturizing powerful laser systems and optics, while the latter two cases inherently require current flow.

To address these limitations, methods of exciting spin waves using applied voltages, rather than electric currents, must be developed. For example, Cherepov *et al.* [15] have demonstrated spin-wave generation and detection in

an artificial multiferroic cell, where voltage contacts are used to create localized radiofrequency stresses in a piezoelectric layer, which then excite spin waves in a coupled magnetic channel via the inverse-magnetostrictive effect. Alternatively, to avoid the complex electrical contacting required for local actuation of a multiferroic system, one may attempt to use inverse magnetostriction to couple spin waves to surface acoustic waves (SAWs). SAWs have similar frequencies to spin waves at the micro- and nanoscales and can be excited by applying high-frequency voltages to interdigitated transducers mounted to the surface of suitable piezoelectric substrates. Furthermore, because SAWs exhibit low propagation losses, one can envisage using a single transducer pair to coherently and efficiently excite spin waves in a large number of channels simultaneously, in a manner that would be beneficial for future magnonic technologies. Previous studies have shown the feasibility of using SAWs to excite ferromagnetic resonance [16–22] and to create subresonance dynamics [23–28] in thin films and nanostructures. However, the coupling of SAWs to the complex spin-wave spectra of magnetic nanostructures has not yet been comprehensively explored, with only the work of Yahagi *et al.* [29] making passing reference to the fact that localized resonant modes can be excited in this way.

---

*raanan.tobey@gmail.com

In this paper, we use time-resolved Faraday rotation measurements and micromagnetic simulations to examine the coupling between the surface acoustic waves and spin-wave modes of an array of nickel nanowires. Our data reveal the strong excitation of magnetization dynamics at applied fields, where either of the nanowire's two primary spin-wave modes is coincident with the frequency of a SAW excited by the optical-pump pulse. Micromagnetic simulations show these two modes to be spatially localized in the body and edges of the nanowire, respectively, thus verifying the feasibility of using SAWs to selectively excite localized spin waves in magnetic nanostructures.

II. METHODOLOGY

Large-area arrays of rectangular-profile nickel nanowires are fabricated on glass (N-BK7) wafers using electron-beam lithography, thermal evaporation, and lift-off processing. The arrays characterized in this study have widths of 250 nm, thicknesses of 40 nm, and periods of 500 nm. The length of the wires is several millimeters and they extend beyond the aperture of the excitation and detection beams. Equivalently evaporated continuous thin films are characterized using a vector-network-analyzer ferromagnetic-resonance (VNAFMR) system. The film's saturation magnetization, $M_s = 315$ kA/m, is found by fitting the variation of the film's resonance frequency with applied field to the Kittel equation, while the variation of the resonance line width with frequency allows the determination of its damping parameter, $\alpha = 0.04$ [30]. We note that the value of M_s is lower than that for bulk nickel, perhaps indicating some oxidation of the uncapped films. Atomic-force-microscopy (AFM) data illustrating the geometry of the array are shown in Fig. 1(a), including an inset line cut showing the uniformity of the final structures.

A schematic diagram illustrating the experimental geometry is presented in Fig. 1(b). Excitation of the nanowire array is achieved by approximately 100-fs optical pulses with wavelength $\lambda_{\text{pump}} = 400$ nm directed at near-normal incidence onto the sample surface. The nanowire's magnetic response is characterized via the Faraday rotation of a time-delayed, linearly polarized probe beam (approximately 100-fs pulses, $\lambda_{\text{probe}} = 800$ nm), directed at normal incidence onto the sample surface. An analysis of the probe beam's polarization using standard polarization bridge techniques as a function of time delay thus allows elucidation of the nanowire's magnetization dynamics. The diameter of the pump beam is several hundred microns (fluence of approximately 5 mJ/cm^2), with the probe beam being fully contained within the pump, meaning that a large number of nanowires are characterized simultaneously. The measurements are performed within the poles of an electromagnet that can be continuously rotated around the sample normal
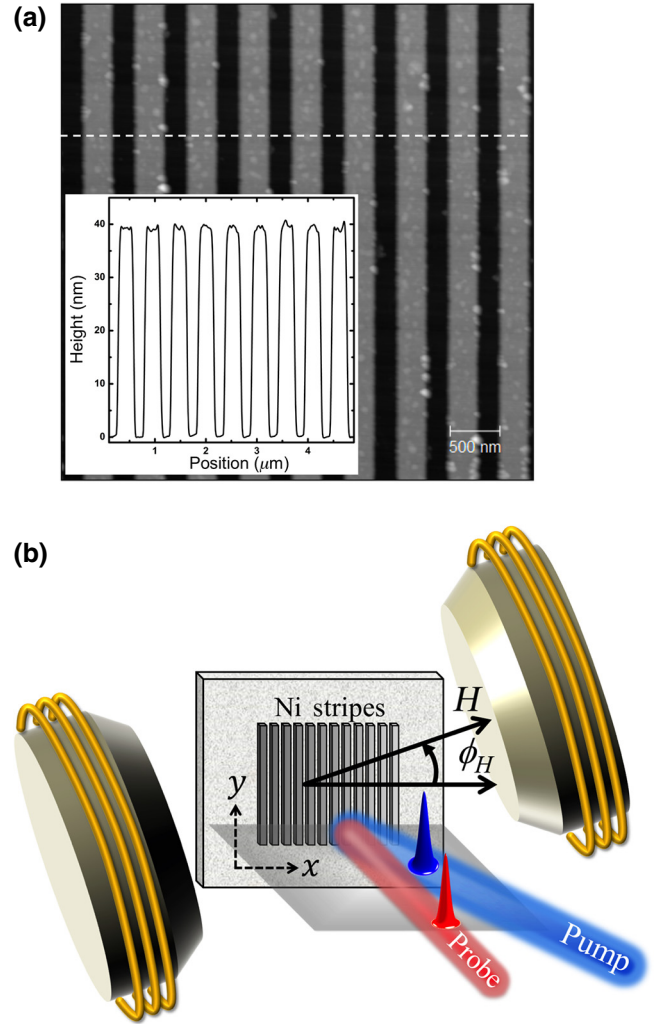

FIG. 1. (a) Atomic-force-microscopy image of the nickel-nanowire array. The inset plot shows a line scan taken along the dashed white line. (b) Schematic diagram indicating the setup of the pump-probe Faraday measurements, including the magnetic-field angle with respect to the array wave vector.

to vary ϕ_H, the angle between the applied field H and the array's wave vector.

Micromagnetic simulations of the nanowire's magnetization dynamics are performed using the MUMAX3 software package [31]. We model a single 500-nm (width) ×1000-nm (length) section of the array and employ periodic boundary conditions in both in-plane directions to emulate both the array's periodicity and the long lengths of the nanowires. A $5 \times 5 \times 5$-nm^3 mesh is used for all simulations. Values of M_s and α are chosen to align the material properties of simulated nanowires with those measured via VNAFMR from continuous films, while the exchange stiffness is set to a standard value of $D_{\text{ex}} = 9$ pJ/m. We neglect the effects of magnetocrystalline anisotropy due to the polycrystalline nature of the experimental samples. To simulate the nanowire's spin-wave spectrum

under given applied field conditions, we first initialize the nanowire's magnetization along a vector $(H_x, H_y, H_z) = (1, 1, 0)$ before relaxing it under the required values of H and ϕ_H. We then apply an abrupt 20 Oe out-of-plane field pulse in order to excite magnetization dynamics within the nanowire and Fourier transform the resulting time-domain data for M_z/M_s (i.e., the out-of-plane component of magnetization) to obtain the nanowire's frequency-domain response. The localization of spin-wave modes is then examined by exciting the array with frequency-matched, sinusoidally varying, out-of-plane applied fields with amplitudes of 10 Oe.

III. RESULTS

Figure 2 presents time- and frequency-domain experimental data for $\phi_H = 10°$, $20°$, and $30°$, along with micromagnetically simulated frequency-domain data. The top row of panels (a)–(c) shows the background-subtracted time-resolved Faraday signals at these magnetic-field angles, which are accompanied by their Fourier transforms in (d)–(f). The time-delay data exhibit complex oscillatory dynamics of the average magnetic moment of the ensemble of Ni wires. In combination with the frequency domain representation, we can understand their salient features.

Two mechanisms for inducing magnetization dynamics are activated when the pump pulse excites the nanowire array. First, fast demagnetization processes suppress [32] the magnetic moment of individual wires, modifying the spatial distribution of their demagnetizing fields and, thus, reorienting the effective magnetic field relative to the applied external field. This process is equivalent to that first demonstrated by van Kampen et al. [33] and results in the frequency-domain data presenting a faint trace of the nanowire's full spin-wave spectrum [Figs. 2(d)–2(f)]. This can be seen most easily by comparing the experimental frequency-domain data [Figs. 2(d)–2(f)] with the simulation results [Figs. 2(g)–2(i)], which show the nanowire's response to a sharp perturbation of the effective field. This simulated response is also overlayed onto the frequency-domain data [the red lines in Figs. 2(d)–2(f)] and shows good quantitative agreement with the experimental results for the displayed angles. We note that, at high applied fields, the nanowire's spin-wave spectrum shows two clear branches for low angles of the magnetic field, ϕ_H. As this angle increases and the field aligns more with the long axis of the wires, the splitting between the two observed resonance branches lessens until, at $30°$, they become nearly indistinguishable.

The second effect of the pump pulse is the excitation of acoustic waves due to the spatially varying optical absorption, and thus spatially varying thermomechanical stress, of the nanowire, a process that is known to lead to excitation of Rayleigh SAWs and the individual
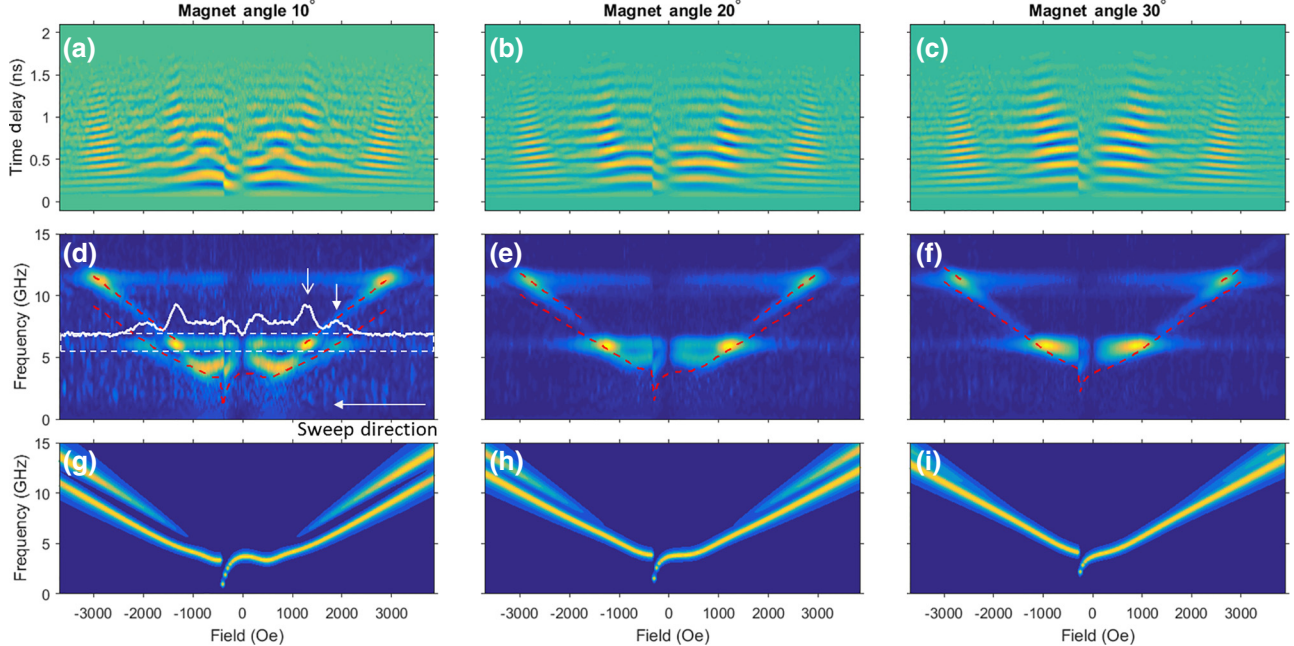

FIG. 2. (a)–(c) Time-domain pump-probe Faraday measurements of the nickel-nanowire array for $\phi_H = 10°$, $20°$, and $30°$. (d)–(f) Equivalent frequency-domain measurements. Red dashed lines indicate the peak positions of the spin-wave spectrum as derived from the results of micromagnetic simulations. For $\phi_H = 10°$, the white line indicates the average intensity measured between the two dashed white lines, which encompass the SAW excitation observed at $f = 6$ GHz. (g)–(i) Micromagnetic simulations of the low-energy spin-wave spectrum of the nanowire. At low angles, a split spectrum elucidates the spin-wave amplitudes located in the bulk and edge regions of the wires.

"breathing" modes of the wires (i.e., both in-plane and out-of-plane dilation and compression of the wire width and height, respectively). Thus, the elastic dynamics of these wire arrays behave similarly to our previously discussed ultrafast transient-grating (TG) measurements on uniform magnetic films [34,35]. The resultant strain profile is that of a standing acoustic wave with antinodes occurring at the center of the wires and the gaps between them, which is equivalent to the case of two counterpropagating surface acoustic waves. The generated acoustic modes are presented as faint horizontal lines in the frequency-domain data and, based on the periodicity of the wire array and the acoustic velocity of the substrate and wire material, we attributed these to be the Rayleigh SAW excitation at 6 GHz and the wire (width) breathing mode at 11.25 GHz, the latter being closely associated with surface-skimming longitudinal (SSLW) modes of the form we have previously reported [36].

The experimental frequency-domain representation also shows clear "hot spots" whenever an acoustic mode crosses the nanowire's spin-wave spectrum, which we show explicitly for the 10° data as an overlayed line cut on the frequency-domain data [Fig. 2(d)]. We understand this to be the resonant interaction between the underlying acoustic waves and the wire's magnetization under the correct applied field conditions. However, distinct from the dynamics previously demonstrated in our TG measurements [34–36], we draw attention specifically to the fact that, in the case presented here (e.g., $\phi_H = 10°$), two clear hot spots are present at the SAW frequency, namely, resonances at approximately ±1225 and ±1850 Oe (indicated by arrows). The nature of these distinct features is the primary focus of this paper and will be discussed in detail shortly.

The form of the nanowire's frequency-domain data can be understood further by considering Fig. 3, which plots the simulated frequencies [Fig. 3(a)] of the nanowire's spin-wave modes, as well as its global values [Fig. 3(b)] of M_x/M_s and M_y/M_s, as a function of the applied field for $\phi_H = 10°$. At large positive fields, the nanowire is almost entirely saturated along the field direction and presents two well-separated modes, the frequencies of which scale almost linearly with the applied field. The existence of these two modes can also be seen clearly in Fig. 4(a), which presents a line cut through the simulated frequency-domain data at $H = 1500$ Oe.

Micromagnetic simulations of the spatial distributions of each branch of the spin-wave spectrum are shown in Fig. 4(b), for a field of 1500 Oe and driving frequencies of 5.1 and 6.9 GHz. The micromagnetic results are plotted for at different time points for a full oscillation period and show the localized nature of the excitations for different precessional frequencies. For example, Fig. 4(b) demonstrates that the lower-frequency resonance is associated with the spin-wave amplitude localized at the edges of
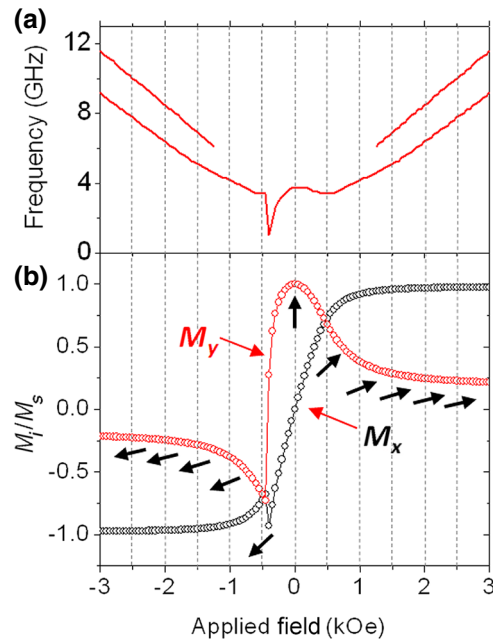

FIG. 3. (a) Peak positions of the nanowire's spin-wave spectrum for $\phi_H = 10°$ as derived from the results of micromagnetic simulations. (b) Corresponding M_x (black circles) and M_y (red circles) components of the nanowire's magnetization as a function of the applied field. The black arrows illustrate the average vector direction of the nanowire's magnetization.

the wire's profile, while the higher-frequency resonances are localized in the centers of the individual wires. The existence of these distinct spatial distributions of the spin waves is the result of nonuniformity of the demagnetizing field across the width of the wire. This field strongly opposes the applied field at the nanowire's edges, lowering the effective field about which the magnetization precesses, and thus decreases the resonant frequency of these regions compared to those in the middle of the nanowires, which form the upper branch on the plot.

Looking again at Fig. 3(b), as the applied field is reduced toward approximately 1000 Oe, the nanowire's magnetization remains closely aligned to the poling direction. However, substantial changes are observed in the frequency-domain data, with the upper branch of the spin-wave spectrum progressively decreasing in intensity relative to the lower branch, such that by $H = 1000$ Oe, the lower branch dominates [Fig. 4(a)]. In this applied field region, the remaining lower branch continues to represent the dynamics of spins at the edges of the nanowire [Fig. 4(c)].

At $H = 500$ Oe, the mode spectrum exhibits a local minimum in frequency as the applied field becomes comparable to the demagnetizing field, minimizing the effective field around which the magnetization precesses. Simultaneously, the reduction in field results in a progressive reorientation of the nanowire's magnetization away
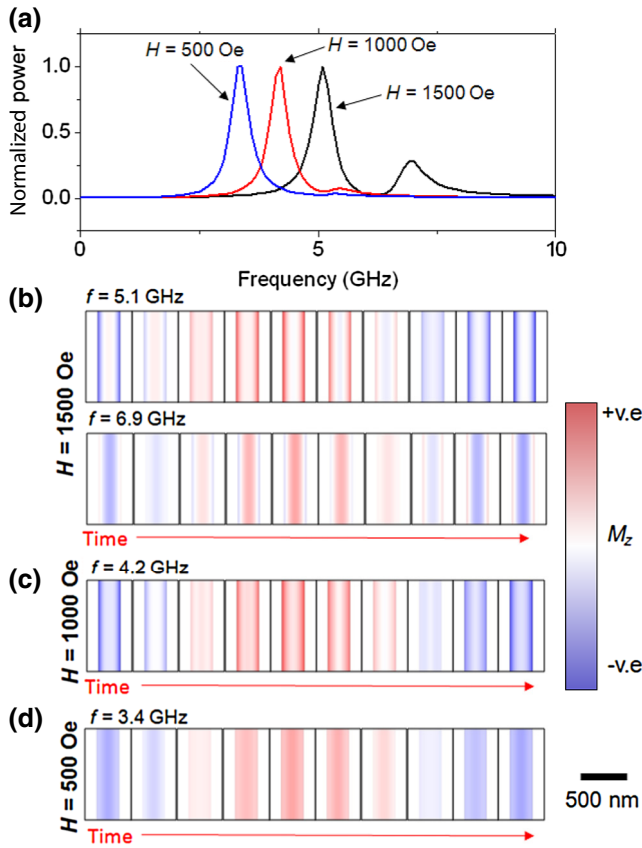
FIG. 4.   (a) Micromagnetically stimulated spin-wave spectra for $H = 500$ (blue), 1000 (red), and 1500 Oe (black) ($\phi_H = 10°$). (b) Micromagnetically stimulated images of the M_z component of magnetization for a complete period of oscillation at $f = 5.1$ GHz and $f = 6.9$ GHz ($H = 1500$ Oe, $\phi_H = 10°$), corresponding to the lower and upper branches of the spin-wave spectrum respectively. (b) Equivalent images for $f = 4.2$ GHz, $H = 1000$ Oe, $\phi_H = 10°$. (c) Equivalent images for $f = 3.4$ GHz, $H = 500$ Oe, $\phi_H = 10°$.

from the hard axes toward their easy axes and an expansion of the remaining mode from the nanowire's edges to the body [Fig. 4(d)]. As the applied field is further reduced to $H = 0$ Oe, the spin-wave frequency increases again due to the nanowire's demagnetizing field becoming dominant over the applied field, resulting in a net increase of the effective field.

For applied fields in the range $H = 0$ Oe to -500 Oe, the mode spectrum first softens and then exhibits a discontinuity at $H = -450$ Oe. These phenomena are attributed to the applied field having developed a component along $-y$, while the magnetization retains a component along $+y$, due to the nanowire's shape anisotropy preventing its reorientation (the wires are initially poled in the positive M direction and so the "flop" transition occurs on the negative M side). The discontinuity in the mode spectrum occurs as the magnetization overcomes this energy barrier to align along $-y$. We note that similar

discontinuities can be observed in the experimental data [Figs. 2(a)–2(c)], albeit at lower fields ($H = -380$ Oe), due to thermal activation assisting the magnetization reorientation in the experiments. For $H < -500$ Oe, the mode spectrum is symmetric with that for equivalent positive fields, indicating that equivalent magnetization dynamics are occurring.

The explanation above can also be applied to understand the variation of the frequency-domain data with ϕ_H shown in Fig. 2. First, as the field angle increases, all spin-wave modes and their elastic resonances shift to smaller applied fields, a general feature associated with the shape anisotropy of the wires [37]. Furthermore, as ϕ_H increases, decreased splitting is observed between the upper and lower branches of the spin-wave spectrum. This decrease can be attributed to the nanowire's magnetization being saturated at larger angles to their hard axes, thus reducing the strength of the demagnetizing field the edge spins experience. The same reduction of the demagnetizing field also explains the reduced prominence of the frequency minima observed for low applied fields as ϕ_H increased.

Having explained the physical origin of the nanowire's spin-wave spectrum, we now return our attention to its coupling to the acoustic excitations generated by the pump pulse. Figures 5(a) and 5(b), respectively, present the negative applied field sections of the time- and frequency-domain data measured for $\phi_H = 10°$. Here, the visibility of the coupling between the SAW and the spin waves in the frequency-domain data [Fig. 5(b)] has been enhanced by applying a two-dimensional Hamming window to the time-delay data [Fig. 5(a)] prior to the Fourier transform being performed. Again, clear hot spots can be observed in the frequency-domain data at the points where the SAW mode
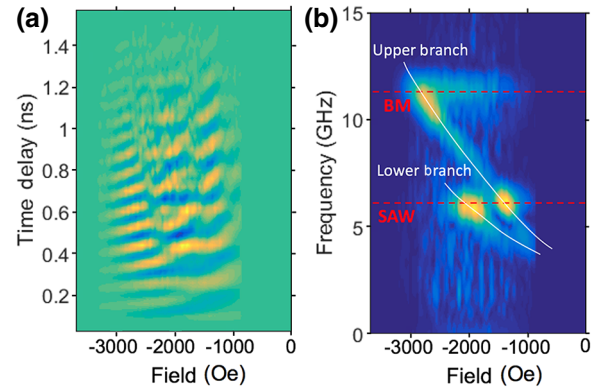

FIG. 5.   (a) Time-domain data for $\phi_H = 10°$ modified by a 2D Hamming window applied in the region where the spin-wave spectrum of the nanowire crosses the SAW and breathing-mode acoustic resonances. (b) Corresponding frequency-domain data. The frequencies of the SAW and breathing-mode (BM) acoustic resonances are indicated by dashed red lines. The white lines are guides for the eye and indicate the frequencies of the upper and lower branches of the spin-wave spectrum.

crosses the previously delineated upper and lower branches of the magnetization dynamics and where the breathing mode crosses its upper branch (our electromagnet prohibited measuring at fields where the breathing mode would be expected to cross the lower branch). The enhancement of the amplitude of the nanowire's magnetization dynamics at these points indicates that a resonant interaction is occurring between elastic and magnetic dynamics. A further signature of this interaction can be seen in the time-domain data of Fig. 5(a), where 180° phase shifts (a tilt in the excitation lobe) are observed as the field is swept through the points of resonance between the SAW mode and spin-wave dynamics.

The key result here is that, depending on the value of the applied magnetic field, the SAW mode resonantly excites either branch of the spin-wave spectrum, which, as we have shown previously, are localized in different sections of the nanowire array. Thus, our measurements provide evidence of the feasibility of selectively exciting localized spin-wave modes by coupling them to acoustic waves.
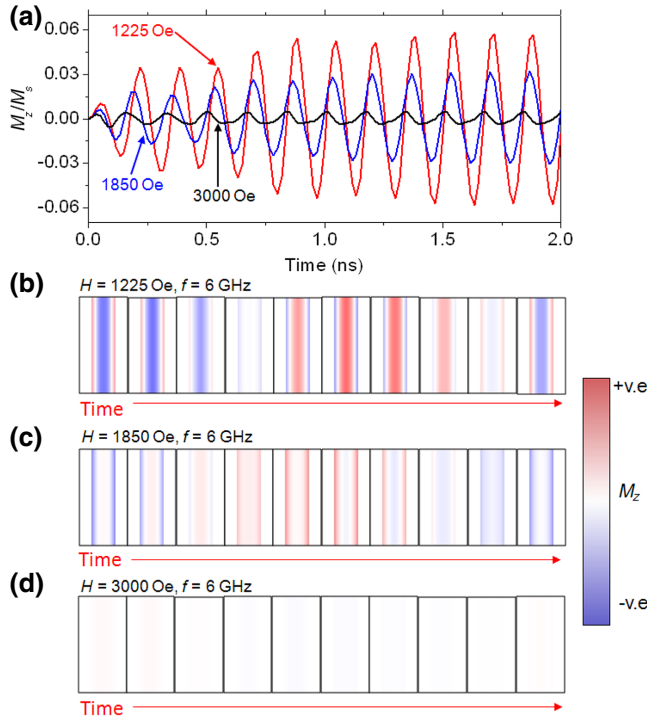
As a final point, we now validate via further simulations the feasibility of acoustically exciting localized spin waves. We begin with the standard equation for the magnetoelastic energy density:

$$E_{\text{M.E.}} = B_1(\epsilon_{xx}m_x^2 + \epsilon_{yy}m_y^2 + \epsilon_{zz}m_z^2)$$
$$+ 2B_2(\epsilon_{xy}m_xm_y + \epsilon_{xz}m_xm_z + \epsilon_{yz}m_ym_z), \quad (1)$$

where B_i are the magnetoelastic coupling constants and ϵ_{ij} are the components of strain that a magnet is subjected to. For an isotropic polycrystalline film $B = B_1 = B_2$ and for a Rayleigh SAW propagating along the x axis, $\epsilon_{yy} = \epsilon_{xy} = \epsilon_{yz} = 0$. For the case of a film thickness much smaller than the SAW wavelength, it is further the case that $\epsilon_{xx} > \epsilon_{xz}, \epsilon_{zz}$ in the near-surface region [38], while the in-plane applied field ensures that $m_x \gg m_z$. Hence, for our experimental geometry, we arrive at $E_{\text{M.E.}} = B\epsilon_{xx}(x,t)m_x^2$, such that the magnetoelastic effects of the SAW are analogous to a spatially and temporally varying uniaxial anisotropy oriented along the x axis. We note that this simple form of excitation was previously used by Weiler *et al.* to reproduce the characteristics of SAW-induced FMR [18], giving us confidence in the validity of our approach.

On the basis of the treatment above, we perform micromagnetic simulations where the Ni nanowires are subjected to a spatial and temporally varying uniaxial anisotropy profile of the form

$$K_1 = B\epsilon_{xx}\cos(2\pi x/\lambda_a)\sin(2\pi f_{\text{saw}}t), \quad (2)$$

where λ_a is the array repeat period ($\lambda_a = 500$ nm), f_{saw} is the frequency of the optically excited SAW as measured from the experimental data ($f_{\text{saw}} = 6$ GHz), $B \sim 7.85$ MJ/m^3, and $\epsilon_{xx} \sim 200$ ppm [19]. While we believe the experimental strains to be larger than this value, micromagnetic simulations are conducted at this reduced strain to ensure the linearity of the simulated results, while the experimental results do not show responses that would be associated with the frequency-mixing phenomena we reported previously [39]. The anisotropy axis is applied along the x axis of the array. The SAWs antinode are located in the center of the nanowires and in the center of the gaps between them. Simulations are performed at three applied fields: $H = 1225$, 1850, and 3000 Oe, corresponding to situations where the upper branch, lower branch, and neither branch of the spin spectrum, respectively, is in resonance with the SAW ($\phi_H = 10°$).

Figure 6(a) presents M_z/M_s (M_z is the measured quantity in the Faraday geometry) vs time for each of the applied fields listed above. As the simulations are started from a stable configuration, the data show an initial period where the dynamics increase in size, before stabilizing as they reach the equilibrium amplitude. For the two cases where the SAW is in resonance with the spin-wave spectrum ($H = 1225$ and 1850 Oe), strong excitation of

FIG. 6. (a) Plots of M_z/M_s vs time for micromagnetic simulations where the nanowire's magnetization is excited by a SAW resonance at $f = 6$ GHz. Data are shown for $H = 1225$ (red), 1850 (blue), and 3000 Oe (black), which correspond to the upper branch of the spectrum being in resonance with the SAW, the lower branch being in resonance, and neither branch being in resonance, respectively. (b)–(d) Corresponding images of the M_z component of magnetization for a complete period of the acoustic excitation.

magnetization dynamics is observed, whereas for $H = 3000$ Oe, where the acoustic excitation is off resonance, only minor perturbations occur. Corresponding spatial-resolved images of the magnetization dynamics [Figs. 6(c) and 6(d)] confirm that the localization of the spin-wave modes is retained under acoustic excitation, with the mode observed at $H = 1225$ Oe localizing in the center of the nanowire and the mode at 1850 Oe localizing at its edges. Together with the experimental data, this result provides strong evidence that surface acoustic waves can be used to selectively excite localized spin-wave dynamics and we expect that a spatially resolved measurement, for example, using time-resolved x-ray photoelectron emission microscopy (XPEEM) [40], would validate these findings.

IV. CONCLUSIONS

In this paper, we use the results of the pump-probe time-resolved Faraday effect and micromagnetic simulations to demonstrate the feasibility of acoustically exciting localized spin waves in nickel nanowires. When saturated (nearly) perpendicular to the nanowire's length, the spin-wave spectrum splits into two modes, respectively localized in the body and at the edges of the nanowires. These modes are determined to be selectively excited when the applied field is tuned so as to bring them into resonance with a surface acoustic wave produced by the pump pulses' interaction with the nanowire's spatially varying thermal absorption.

Our work paves the way for future devices in which surface acoustic waves can be used to coherently excite spin waves in magnonic logic devices, e.g., by selectively exciting localized modes in nanowire end domains, which then in turn act as sources for propagating spin waves. Further applications could include spin-wave amplification, boosting capabilities for long-distance spin-wave transmission in the absence of Joule heating in the generation, and amplification processes. An important step in achieving such advances will be reproducing our results in devices where spin waves are excited by surface-mounted interdigitated transducers (either in the standing-wave or traveling-wave configurations), thus demonstrating a true device implementation of the approach we propose.

[1] M. M. Waldrop, The chips are down for Moore's law, Nat. News **530**, 144 (2016).

[2] V. V. Kruglyak, S. O. Demokritov, and D. Grundler, Magnonics, J. Phys. D: Appl. Phys. **43**, 264001 (2010).

[3] M. Krawczyk and D. Grundler, Review and prospects of magnonic crystals and devices with reprogrammable band structure, J. Phys.: Condens. Matter **26**, 123202 (2014).

[4] Y. Au, M. Dvornik, T. Davison, E. Ahmad, P. S. Keatley, A. Vansteenkiste, B. Van Waeyenberge, and V. V. Kruglyak, Direct Excitation of Propagating Spin Waves by Focused Ultrashort Optical Pulses, Phys. Rev. Lett. **110**, 097201 (2013).

[5] T. Satoh, Y. Terui, R. Moriya, B. A. Ivanov, K. Ando, E. Saitoh, T. Shimura, and K. Kuroda, Directional control of spin-wave emission by spatially shaped light, Nat. Photonics **6**, 662 (2012).

[6] A. Kamimaki, S. Iihama, Y. Sasaki, Y. Ando, and S. Mizukami, Micro-focused pulse laser-induced propagating spin waves in permalloy films with different thicknesses, IEEE Trans. Magn. **53**, 1 (2017).

[7] S. Iihama, Y. Sasaki, A. Sugihara, A. Kamimaki, Y. Ando, and S. Mizukami, Quantification of a propagating spin-wave packet created by an ultrashort laser pulse in a thin film of a magnetic metal, Phys. Rev. B **94**, 020401 (2016).

[8] Y. Hashimoto, S. Daimon, R. Iguchi, Y. Oikawa, K. Shen, K. Sato, D. Bossini, Y. Tabuchi, T. Satoh, B. Hillebrands *et al.*, All-optical observation and reconstruction of spin wave dispersion, Nat. Commun. **8**, 15859 (2017).

[9] T. Schwarze and D. Grundler, Magnonic crystal wave guide with large spin-wave propagation velocity in CoFeB, Appl. Phys. Lett. **102**, 222412 (2013).

[10] Y. Au, E. Ahmad, O. Dmytriiev, M. Dvornik, T. Davison, and V. V. Kruglyak, Resonant microwave-to-spin-wave transducer, Appl. Phys. Lett. **100**, 182404 (2012).

[11] P. Gruszecki, M. Kasprzak, A. E. Serebryannikov, M. Krawczyk, and W. Smigaj, Microwave excitation of spin wave beams in thin ferromagnetic films, Sci. Rep. **6**, 22367 (2016).

[12] V. E. Demidov, S. Urazhdin, R. Liu, B. Divinskiy, A. Telegin, and S. O. Demokritov, Excitation of coherent propagating spin waves by pure spin current, Nat. Commun. **7**, 10446 (2016).

[13] M. Madami, S. Bonetti, G. Consolo, S. Tacchi, G. Carlotti, G. Gubbiotti, F. B. Mancoff, M. A. Yar, and J. Akerman, Direct observation of a propagating spin wave induced by spin-transfer torque, Nat. Nanotechnol. **6**, 635 (2011).

[14] V. E. Demidov, S. Urazhdin, and S. O. Demokritov, Direct observation and mapping of spin waves emitted by spin-torque nano-oscillators, Nat. Mater. **9**, 984 (2010).

[15] S. Cherepov, P. Khalili Amiri, J. G. Alzate, K. Wong, M. Lewis, P. Upadhyaya, J. Nath, M. Bao, A. Bur, T. Wu *et al.*, Electric-field-induced spin wave generation using multiferroic magnetoelectric cells, Appl. Phys. Lett. **104**, 082403 (2014).

[16] A. Comin, C. Giannetti, G. Samoggia, P. Vavassori, D. Grando, P. Colombi, E. Bontempi, L. E. Depero, V. Metlushko, B. Ilic *et al.*, Elastic and Magnetic Dynamics of Nanomagnet-Ordered Arrays Impulsively Excited by

Subpicosecond Laser Pulses, Phys. Rev. Lett. **97,** 217201 (2006).

[17] N. Ogawa, W. Koshibae, A. J. Beekman, N. Nagaosa, M. Kubota, M. Kawasaki, and Y. Tokura, Photodrive of magnetic bubbles via magnetoelastic waves, Proc. Natl. Acad. Sci. **112,** 8977 (2015).

[18] M. Weiler, H. Huebl, F. S. Goerg, F. D. Czeschka, R. Gross, and S. T. B. Goennenwein, Spin Pumping with Coherent Elastic Waves, Phys. Rev. Lett. **108,** 176601 (2012).

[19] L. Dreher, M. Weiler, M. Pernpeintner, H. Huebl, R. Gross, M. S. Brandt, and S. T. B. Goennenwein, Surface acoustic wave driven ferromagnetic resonance in nickel thin films: Theory and experiment, Phys. Rev. B **86,** 134415 (2012).

[20] L. Thevenard, C. Gourdon, J. Y. Prieur, H. J. von Bardeleben, S. Vincent, L. Becerra, L. Largeau, and J. Y. Duquesne, Surface-acoustic-wave-driven ferromagnetic resonance in (Ga,Mn)(As,P) epilayers, Phys. Rev. B **90,** 094401 (2014).

[21] P. G. Gowtham, T. Moriyama, D. C. Ralph, and R. A. Buhrman, Traveling surface spin-wave resonance spectroscopy using surface acoustic waves, J. Appl. Phys. **118,** 233910 (2015).

[22] P. Kuszewski, J.-Y. Duquesne, L. Becerra, A. Lemaître, S. Vincent, S. Majrab, F. Margaillan, C. Gourdon, and L. Thevenard, Optical probing of Rayleigh wave driven magneto-acoustic resonance, https://arxiv.org/abs/1806.11410 (2018).

[23] S. Davis, A. Baruth, and S. Adenwalla, Magnetization dynamics triggered by surface acoustic waves, Appl. Phys. Lett. **97,** 232507 (2010).

[24] S. Davis, J. A. Borchers, B. B. Maranville, and S. Adenwalla, Fast strain wave induced magnetization changes in long cobalt bars: Domain motion versus coherent rotation, J. Appl. Phys. **117,** 063904 (2015).

[25] W. Li, B. Buford, A. Jander, and P. Dhagat, Magnetic recording with acoustic waves, Phys. B: Condens. Matter **448,** 151 (2014).

[26] J. Dean, M. Bryan, J. Copper, A. Virbule, J. Cunningham, and T. Hayward, A sound idea: Manipulating domain walls in magnetic nanowires using surface acoustic waves, Appl. Phys. Lett. **107,** 142405 (2015).

[27] L. Thevenard, I. S. Camara, J. Y. Prieur, P. Rovillain, A. Lemaitre, C. Gourdon, and J. Y. Duquesne, Strong reduction of the coercivity by a surface acoustic wave in an out-of-plane magnetized epilayer, Phys. Rev. B **93,** 140405 (2016).

[28] K. Roy, S. Bandyopadhyay, and J. Atulasimha, Hybrid spintronics and straintronics: A magnetic technology for ultra low energy computing and signal processing, Appl. Phys. Lett. **99,** 063108 (2011).

[29] Y. Yahagi, C. Berk, B. Hebler, S. Dhuey, S. Cabrini, M. Albrecht, and H. Schmidt, Optical measurement of damping in nanomagnet arrays using magnetoelastically driven resonances, J. Phys. D: Appl. Phys. **50,** 17LT01 (2017).

[30] S. S. Kalarickal, P. Krivosik, M. Wu, C. E. Patton, M. L. Schneider, P. Kabos, T. J. Silva, and J. P. Nibarger, Ferromagnetic resonance linewidth in metallic thin films: Comparison of measurement methods, J. Appl. Phys. **99,** 093909 (2006).

[31] A. Vansteenkiste, J. Leliaert, M. Dvornik, M. Helsen, F. Garcia-Sanchez, and B. Van Waeyenberge, The design and verification of MuMax3, AIP Adv. **4,** 107133 (2014).

[32] E. Beaurepaire, J.-C. Merle, A. Daunois, and J.-Y. Bigot, Ultrafast Spin Dynamics in Ferromagnetic Nickel, Phys. Rev. Lett. **76,** 4250 (1996).

[33] M. van Kampen, C. Jozsa, J. Kohlhepp, P. LeClair, L. Lagae, W. de Jonge, and B. Koopmans, All-Optical Probe of Coherent Spin Waves, Phys. Rev. Lett. **88,** 227201 (2002).

[34] J. Janušonis, C. L. Chang, P. H. M. van Loosdrecht, and R. I. Tobey, Frequency tunable surface magneto elastic waves, Appl. Phys. Lett. **106,** 181601 (2015).

[35] J. Janušonis, T. Jansma, C. L. Chang, L. Q. A. Gatilova, A. M. Lomonosov, V. Shalagatskyi, T. Pezeril, V. V. Temnov, and R. I. Tobey, Transient grating spectroscopy in magnetic thin films: Simultaneous detection of elastic and magnetic dynamics, Sci. Rep. **6,** 29143 (2016).

[36] J. Janušonis, C. L. Chang, T. Jansma, A. Gatilova, V. S. Vlasov, A. M. Lomonosov, V. V. Temnov, and R. I. Tobey, Ultrafast magnetoelastic probing of surface acoustic transients, Phys. Rev. B **94,** 024415 (2016).

[37] J. Berendt, J. Teixeira, A. Garcia-Garcia, M. Raposo, P. Ribeiro, J. Dubowik, G. Kakazei, and D. Schmool, Tunable magnetic anisotropy in permalloy thin films grown on holographic relief gratings, Appl. Phys. Lett. **104,** 082408 (2014).

[38] G. Farnell and E. Adler, *Physical Acoustics* (Academic Press, New York, 1972), Vol. 9, p. 35.

[39] C. L. Chang, A. M. Lomonosov, J. Janušonis, V. S. Vlasov, V. V. Temnov, and R. I. Tobey, Parametric frequency mixing in a magnetoelastically driven linear ferromagnetic-resonance oscillator, Phys. Rev. B **95,** 060409(R) (2017).

[40] M. Foerster, F. Macià, N. Statuto, S. Finizio, A. Hernández-Mínguez, S. Lendínez, P. V. Santos, J. Fontcuberta, J. M. Hernàndez, M. Kläui *et al.*, Direct imaging of delayed magneto-dynamic modes induced by surface acoustic waves, Nat. Commun. **8,** 407 (2017).